Available online at www.sciencedirect.com
ScienceDirect
Proceedings of the Combustion Institute 33 (2011) 549–557
Proceedings of the Combustion Institute
www.elsevier.com/locate/proci

Experimental and numerical study of soot formation in laminar ethylene diffusion flames at elevated pressures from 10 to 35 atm

Marc R.J. Charest *, Hyun I. Joo, Ömer L. Gülder, Clinton P.T. Groth

University of Toronto Institute for Aerospace Studies, 4925 Dufferin Street, Toronto, Ontario, Canada M3H 5T6

Available online 24 September 2010

Abstract

The effects of pressure on soot formation and flame structure were studied experimentally and numerically in coflow ethylene–air laminar diffusion flames between 10 and 35 atm. Reliable measurements up to 35 atm were permitted by diluting the fuel with nitrogen and suppressing smoke formation. These measurements were compared with numerical predictions to assess the accuracy of current soot models applied to high pressure diffusion flames. The numerical framework used in the present work represents the current state of the art in computational modelling, making use of a block-based parallel implicit finite-volume scheme and detailed radiation heat transfer. In the current implementation, a semi-empirical acetylene-based model is used to predict the nucleation, growth, and oxidation of soot particles. Although the soot model is based on experimental data at atmospheric pressure, it correctly predicted many of the observed trends with pressure. A narrowing flame with constant height was observed as pressure was increased in both the experiments and numerical results. The model also captured the observed relationship between the maximum amount of carbon converted to soot and pressure, although soot volume fractions were generally over-predicted everywhere in the flames. In both the experiments and predictions, soot volume fractions increased with pressure while the tendency of the fuel to produce more soot declined as pressure was increased. Interestingly, the calculations predicted soot inside the fuel tube at 20 atm whose concentrations increased with pressure. An analysis of the numerical results concluded that this early appearance of soot was attributed to fuel pyrolysis inside the tube which accelerated as pressure was increased from 10 to 35 atm.

Keywords: Soot formation; High pressure combustion; Ethylene diffusion flames; Soot modelling

1. Introduction

Pressure has a profound effect on the overall soot yield as well as the rates of soot production and oxidation in diffusion flames. Our current understanding of the effects of pressure on soot formation and oxidation is limited as most experimental and numerical studies have focused on atmospheric flames. On the other hand, practical combustion devices such as gas turbine combustors and diesel engines operate at elevated pressures.

Despite the challenges associated with measuring soot concentrations in high pressure laminar

* Corresponding author. Fax: +1 416 667 7799.
E-mail address: charest@utias.utoronto.ca (M.R.J. Charest).

1540-7489/$ - see front matter © 2010 The Combustion Institute. Published by Elsevier Inc. All rights reserved.
doi:10.1016/j.proci.2010.07.054

diffusion flames, several studies at pressures above atmospheric exist. Flower and Bowman [1] measured the line-of-sight integrated soot volume fraction in ethylene flames between 1 and 10 atm. They found that the maximum value reached in each flame scaled with pressure raised to an exponent of 1.2. Lee and Na [2] obtained a similar result for ethylene flames between 1 and 4 atm. More recently, the path-integrated and local soot volume fractions were measured in methane flames between 1 and 25 atm and ethylene flames between 1 and 16 atm by McCrain and Roberts [3]. Thomson et al. [4] obtained radially-resolved measurements for soot concentration and temperature in methane–air diffusion flames from 5 to 40 atm. This work was continued to include measurements up to 60 atm by Joo and Gülder [5]. Similar experiments were performed by Bento et al. [6] with propane–air flames up to 7.3 atm.

There are many numerical studies on soot formation in laminar diffusion flames at atmospheric pressure [7–11] but only a few at elevated pressures [12,13]. The detailed numerical study by Liu et al. [13] on methane–air diffusion flames between 5 and 40 atm concluded that the increase in soot production with increasing pressure was due to larger mixture densities and higher species concentrations. Increasing pressure was also observed to enhance air entrainment into the fuel stream near the burner tip, accelerating the pyrolysis of fuel. The study showed large discrepancies between measurements and predictions which were attributed to the inability of simplified soot formation/destruction models to accurately predict soot concentrations. However, the fuel preheating effect, which is known to significantly affect numerical predictions [14], was neglected in the study.

In the present research, laminar diffusion flames of ethylene were studied both experimentally and numerically between 10 and 35 atm to investigate the effect of pressure on soot formation and oxidation. Radially resolved measurements for both soot volume fraction and temperature were obtained and compared with the numerical predictions to assess the accuracy of simplified soot models applied to high pressure diffusion flames. With the help of the numerical results, some of the observed phenomena are discussed.

2. Experimental methodology

The experimental apparatus consists of a coflow burner installed inside a pressure vessel that allows the burner operating pressure to be varied as desired. This apparatus is described in detail elsewhere [4,6,5]. The burner consists of a stainless steel central fuel tube with 3 mm inner diameter and a concentric tube of 25.4 mm inner diameter that supplies the coflow air. The outer surface of the fuel tube is chamfered to form a knife-edge at the nozzle exit plane. While this was necessary to improve flame stability over a wide range of pressures, uncertainties in the fuel's outlet velocity profile are introduced as a result. A chimney was also installed to improve flame stability by shielding the core flow from disturbances created inside the chamber.

Line-of-sight measurements using the spectral soot emission diagnostic (SSE) technique were used to construct radial profiles for temperature and soot volume fraction at different axial heights along the burner axes. The theory and configuration of the present SSE system is well documented [15,4,6,5].

Ethylene was diluted with nitrogen to inhibit smoke formation and allow reliable measurements up to pressures of 35 atm. Above this pressure, the flames became unstable and meaningful measurements were no longer possible. The lowest pressure investigated was limited to 10 atm since the SSE technique requires strong radiation from soot to work properly. Ethylene and nitrogen were supplied through the fuel tube at 0.27 and 1.35 mg/s, respectively, while coflow air was supplied at 0.4 g/s. This ethylene flow rate corresponds to an equivalent carbon flow rate of 0.231 mg/s. These mass flow rates were maintained throughout the study while measurements were obtained at 10, 20, 30, and 35 atm in height increments of 0.5 mm and radial increments of 50 μm.

3. Numerical model

A numerical framework previously developed by Charest et al. [16,17] for the solution of laminar reacting flows with complex chemistry, non-gray radiative heat transfer, and soot was applied to study the flames described in the previous section. This framework solves the conservation equations for continuous, multi-component compressible gas mixtures [18]. Soot is modelled using the approach proposed by Leung et al. [19] which requires only two additional transport equations for soot mass and number. These authors described the evolution of soot through four basic steps—nucleation, surface growth, coagulation, and oxidation—and assumed that acetylene is the only precursor responsible for the presence of soot. Surface growth was assumed proportional to the square root of soot particle surface area per unit volume of aerosol. Based on the work of Liu et al. [20,13], this soot model was updated to include oxidation by OH and O since the original model only accounted for O_2 oxidation. All rate constants related to soot were taken from [13].

Multi-species diffusion is modelled here using the first-order Hirschfelder and Curtiss approxi-

mation [21] while soot is assumed to diffuse only by thermophoresis using a model based on the limit of free-molecular flow [22]. A small diffusion coefficient for soot due to particle concentration gradients was included to aid numerical stability even though it is generally negligible. This numerical instability was also observed by Kennedy et al. [23].

Radiation emitted and absorbed by the gas and soot is modelled using the discrete ordinates method (DOM) coupled with the point-implicit finite volume approach of Carlson and Lathrop [24]. Spatial derivatives are evaluated using centered differences while ordinate directions and weights were selected based on the T_3 quadrature set [25]. Spectral absorption coefficients are approximated by the statistical narrow-band correlated-k (SNBCK) model developed by Liu et al. [26]. Four Gauss quadrature points were found to provide a reasonable balance between accuracy and computational expense [27,28]. In this work, the narrow-band data of Soufiani and Taine [29] for H_2O, CO_2, and CO are used to construct the cumulative distribution function. To reduce the number of unknowns required for non-gray radiation in mixtures, the three radiating gases are approximated by a single gas with effective narrow-band parameters based on the optically thin limit [30]. Additional computational savings are achieved by combining bands to form several wide bands using the lumping procedure described by Liu et al. [26]. Based on the recommendations of Goutière et al. [31], a total of nine non-uniformly spaced wide bands are employed. The soot absorption coefficient is determined in the Rayleigh limit for small spherical particles [20].

The governing equations are solved numerically using a finite-volume scheme previously developed by Groth and co-workers [32,33]. The scheme makes use of piecewise limited linear reconstruction and an approximate Riemann solver to determine the inviscid fluxes [34]. The viscous fluxes were evaluated using the second-order diamond-path method developed by Coirier and Powell [35]. Both the inviscid flux and the temporal derivative are preconditioned using the proposed matrix of Weiss and Smith [36]. This preconditioning helps reduce excessive dissipation and numerical stiffness commonly encountered when applying the compressible gas equations to low-Mach-number flows. The solution of the fully-coupled non-linear ODEs is relaxed to a steady-state using the block-based parallel implicit algorithm developed by Northrup and Groth [32] which makes use of a matrix-free inexact Newton–Krylov method. Solution of the DOM equations is decoupled from the gas-particle flow equations and solved sequentially at each time step.

Thermodynamic and transport properties along with gas-phase kinetic rates are evaluated using CANTERA [37], an open-source software package for chemically-reacting flows. The simulations were performed using the skeletal mechanism of Law [38] for ethylene–air combustion which consisted of 33 species and 205 elementary reactions.

4. Discretization and boundary conditions

The modelled domain is shown schematically in Fig. 1 along with the employed boundary conditions. The domain extends radially outwards 10 and 15 mm downstream. The far-field boundary was treated using a free-slip condition which neglects any shear imparted to the coflow air by the chimney walls. The modelled domain is also extended 4.5 mm upstream into the fuel and air tubes to account for the effects of fuel preheating observed by Guo et al. [14] and better represent the inflow velocity distribution. At the outlet, temperature, velocity, species mass fractions, and soot number density are extrapolated while pressure is held fixed. The gas/soot mixture is specified at the inlet along with velocity and temperature while pressure is extrapolated. Uniform velocity and temperature profiles were specified for both the fuel and air inlet boundaries. For the radiation solver, all boundaries except for the axis of symmetry are assumed to be cold and black.

A simplified representation of the fuel tube geometry was employed to reduce the numerical complexity of this particular problem. As shown in Fig. 1, the knife-edge of the fuel tube was approximated by a tube with 0.4 mm thick walls. The three surfaces that lie along the tube wall were modelled as adiabatic walls with zero-slip conditions. Fixed-temperature wall boundary conditions were also tested, however, adiabatic wall conditions provided the best agreement between

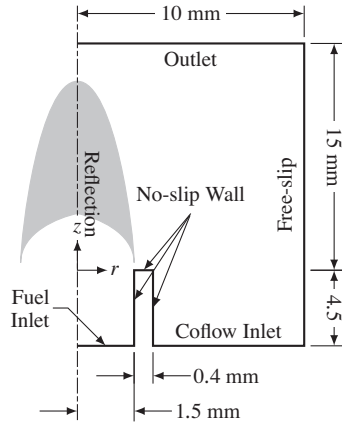

Fig. 1. Computational domain and boundary conditions.

numerical predictions and experimental measurements.

The computational domain illustrated in Fig. 1 was subdivided into 192 cells in the radial- and 320 in the axial-direction to form a structured, non-uniformly-spaced computational mesh of 60,000 total cells. These cells were clustered towards the burner exit plane to capture interactions near the fuel tube walls and towards the centerline to capture the core flow of the flame. A fixed mesh spacing of approximately 18 μm was specified in the radial-direction between $r = 0$ and 2.4 mm. The vertical spacing approaches 5.7 μm near the fuel tube exit plane. Increasing the mesh resolution further did not offer any improvements in accuracy or alter the numerical solution.

5. Experimental and numerical results

Images of the flames over the range of pressures studied are provided in Fig. 2. The shape of the flame and its appearance changes significantly with pressure. Increasing pressure causes the flame diameter to narrow and the luminosity to intensify while the height remains constant at 5.5 mm. At 10 atm, a blue region exists in the lower portion of the flame which suggests the presence of a small premixed zone. As pressure is increased to 20 atm, this blue region diminishes and the yellow luminous region in the upper portion of the flame moves towards burner tip. The blue zone nearly vanishes with further increase in pressure and the flame appears attached to the burner rim, suggesting that soot is formed at the burner exit. Similar observations were made for methane–air flames [4,5].

5.1. Comparison with experiment

Measured radial profiles of soot volume fraction are compared with the calculations in Fig. 3. The model predicts many of the experimentally observed trends but generally over-predicts the soot volume fraction throughout the flames. In both the experiments and calculations, soot is formed in an annulus downstream of the fuel tube rim and the magnitude of the soot volume fraction initially increases with height. The locations of the peaks within this annulus converge towards the centerline as the inner accelerating core flow entrains the soot particles inwards. Oxidative processes begin to convert soot to gaseous CO higher up in the flame and the annular region with high soot levels collapse on the flame axis. As pressure is increased, the location of the peaks in the radial profiles for soot volume fraction contract radially-inwards and the peaks become more pronounced. Soot production also increases with pressure since the higher pressures and contracting flame result in higher gaseous species concentrations and faster reaction rates. While these features are observed in the numerical results, the magnitudes of the predicted soot volume fraction is greatly over-predicted in most cases, especially in the annular region with high soot levels. For example, at a height of 3 mm, soot is over-predicted by factors of 7.0, 2.1, 1.9, and 1.9 in the 10, 20, 30, and 35 atm flames, respectively. At this height, the quantitative agreement improves with pressure. Higher in the flame at $z = 5$ mm, soot is under-predicted for all flames except the 35 atm flame. Despite the disagreement between the magnitudes of the predicted and measured soot concentrations, the model correctly captures the positions of the annuli. The poorest agreement occurs in the 10 atm flame where the numerical peak at 4 mm is shifted outwards.

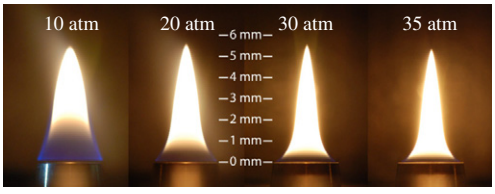

Fig. 2. Flame images at pressures from 10 to 35 atm.

A comparison between the predicted and measured radial temperature profiles is presented in Fig. 3. The same trends with pressure and flame height are observed experimentally and numerically. First, temperature shows an annular structure similar to the radial profiles for soot volume fraction except that the radial location where temperature peaks occurs at a slightly larger radius. With increasing height in the flame, both sets of results show an increase in the peak temperature which gradually shifts in position towards the centerline. The experiments also show that increasing pressure results in lower measured peak temperatures at each height. While the predictions show this same trend, the decrease with pressure is not as severe. The best agreement between the predicted and experimental values for the maximum temperature reached at each height occurs in the 10 atm flame. For all the flames, the largest discrepancies occur at a height of 1 mm. At this height the peaks are over-predicted by 60, 105, and 110 K at 20, 30, and 35 atm, respectively. This over-prediction of temperature low in the flame is attributed to higher predicted wall temperatures which result from the adiabatic boundary conditions. The shifted temperature profiles are most likely caused by the simplified geometry.

To assess the fuel's propensity to soot and its sensitivity to pressure, the variation in the carbon conversion factor with pressure was studied. This factor is defined as $\eta_s = \dot{m}_s/\dot{m}_c$ where $\dot{m}_c$ is the carbon mass flow rate at the nozzle exit [1,4].

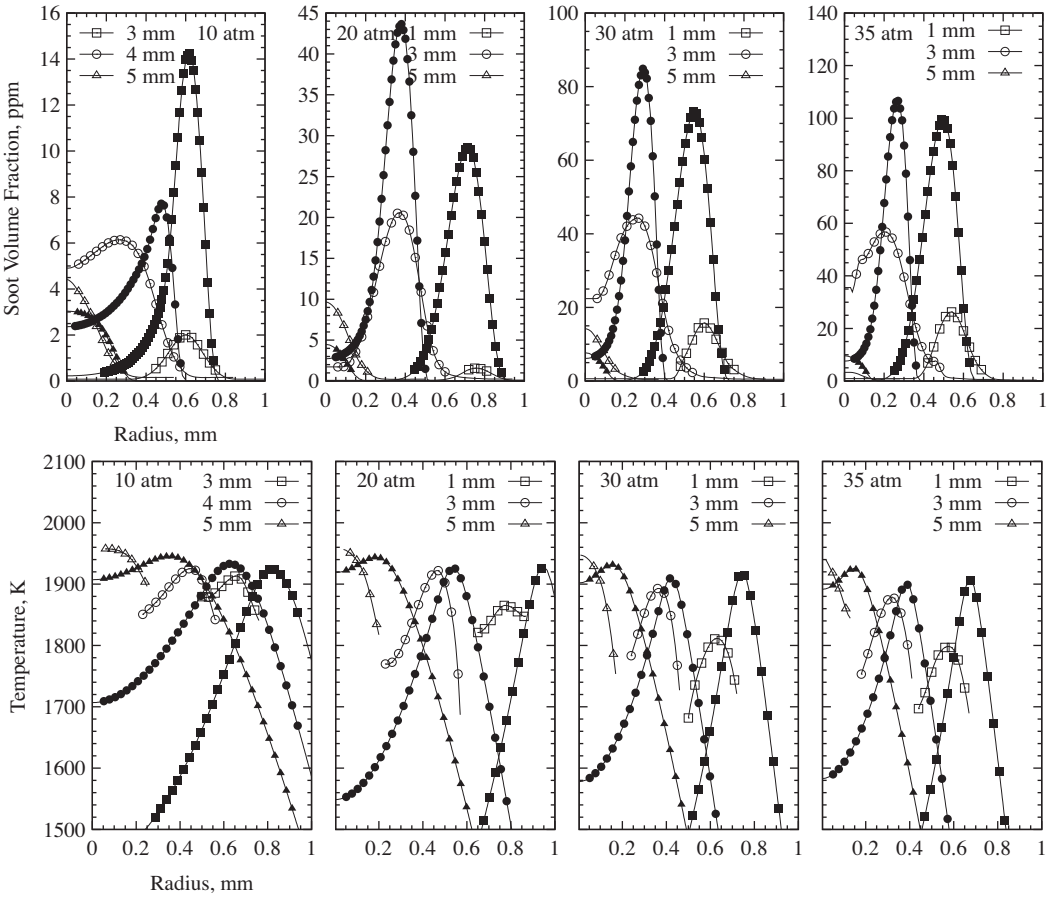

Fig. 3. Measured (open symbols) and predicted (filled symbols) radial profiles for soot volume fraction and temperature.

The mass flux of soot through a horizontal cross-section is $\dot{m}_s = 2\pi\rho_s \int f_v v_z r\,dr$ where $\rho_s = 1.9\ \mathrm{g/cm^3}$ is the density of soot, f_v is the soot volume fraction, and v_z is the axial velocity. Since the velocity is not known in the experiments, it is estimated by $v_z = \sqrt{2az}$ where z is the height above the burner and a is an acceleration constant commonly assumed equal to 25 m/s [39]. As an alternative, v_z is estimated using the computed velocity.

As observed in Fig. 4, there is a significant difference between the two lines corresponding to the experimental results for η_s based on the different velocity approximations. The values computed using the predicted velocity field are assumed to be more accurate.

The predictions for η_s, Fig. 4, mimic the experimentally observed trends although the model consistently over-predicts the maximum η_s in each flame. The peak η_s is over-predicted by factors of 1.8, 1.3, 1.2, and 1.4, at 10, 20, 30, and 35 atm, respectively, when compared with the experimental results computed using the predicted velocity field. Both the experimentally-based and predicted maximum η_s display a power-law dependence on pressure, $\eta_s \propto p^n$, which weakens as pressure is increased from 10 to 35 atm. A more

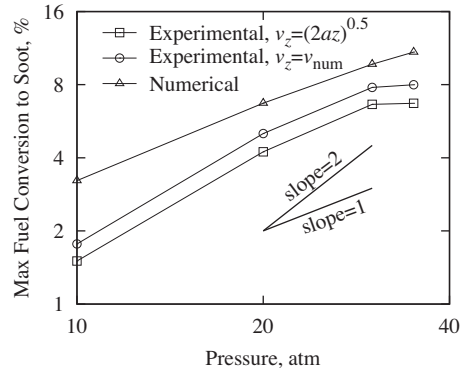

Fig. 4. Measured (open symbols) and predicted (filled symbols) amount of fuel carbon converted to soot.

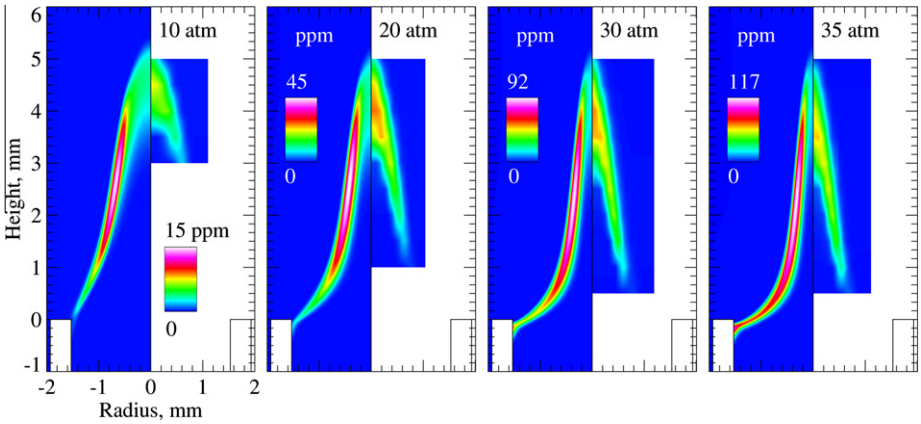

Fig. 5. Predicted (left) and measured (right) contours for soot volume fraction.

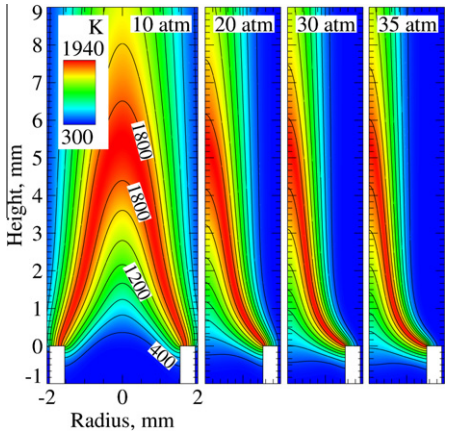

Fig. 6. Predicted contours for temperature.

drastic reduction in the pressure exponent, n, is observed in the experiments.

Two-dimensional contour plots of soot volume fraction were constructed from the measurements and are compared with the numerical results in Fig. 5. Qualitatively, the predicted and measured flame geometries are similar and the narrowing of the flame with increasing pressure is clearly observed in both sets of results. The flame height based on soot volume fraction is also accurately predicted by the model. In the experiments, it is approximately 5 mm and remains constant throughout the entire range of pressures investigated. Similar observations are made for the numerical predictions. However, the model incorrectly predicts the location of the peak soot volume fraction and, in general, some significant differences between predicted and measured soot concentrations can be observed at lower flame heights. Soot is predicted to occur in an annular region low in the flame, whereas experimental observations show that the peak occurs along the centerline near the flame tip. Additionally, the model always predicts that soot production

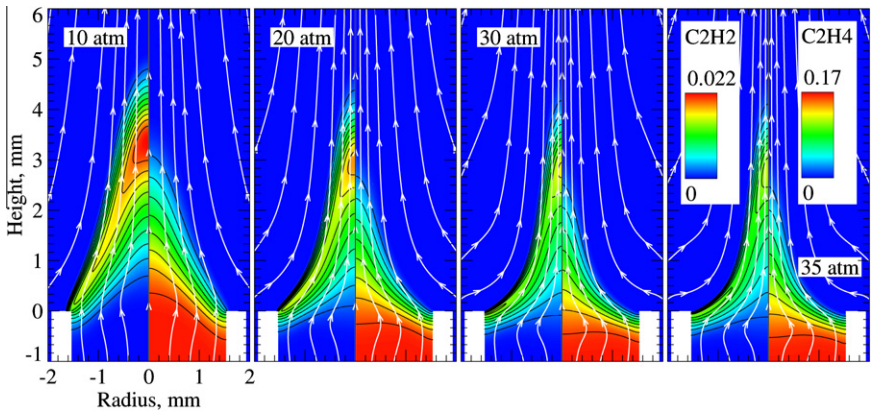

Fig. 7. Predicted contours for C_2H_2 (left) and C_2H_4 (right) mass fraction.

begins further upstream than in the experiments. With increasing pressure, both experiments and predictions show that the initial onset of soot formation begins earlier and that the annular structure becomes thinner and more pronounced. At 20 atm, the model predicts a small amount of soot inside the fuel tube and adjacent to the tube walls. This production of soot inside the tube intensifies as pressure is further increased to 35 atm.

The over-prediction of soot and temperature low in the flame near the burner suggests that the adiabatic wall boundary conditions predict wall temperatures that are too high. Higher temperatures near the wall would increase the rate of fuel pyrolysis and cause the early predicted appearance of soot in Fig. 5. However, it is unclear whether the early formation of soot inside the tube is solely an artifact of over-predicted wall temperatures. This early predicted formation of soot may also be related to inadequacies of the soot model.

5.2. Effects of pressure

Predicted contours of temperature for each flame are presented in Fig. 6. As pressure is increased from 10 to 35 atm, the flame contracts inward and the main attachment point shifts towards the centerline. At 10 atm, the flame is relatively unstrained and attached to the top of the fuel tube wall. This attachment point moves towards the inner edge of the fuel tube as pressures are increased to 35 atm. At 35 atm, the base of the flame is highly strained and significant fuel preheating is observed inside the tube near the walls. There is also a significant increase in the temperature near the centerline just upstream of the fuel tube. Figure 7 presents the predicted contours for C_2H_4 and C_2H_2 mass fraction in the vicinity of the burner rim. At 10 atm, C_2H_4 is partially consumed near the tube walls prior to exiting the fuel nozzle and the concentrations along the centerline remain high for the first 0.5 mm. The rate of C_2H_4 consumption increases significantly as pressure is increased. At 35 atm, most of the fuel is broken down inside the fuel tube and C_2H_4 concentrations along the inner tube walls are completely depleted before leaving the mouth of the burner. Ethylene concentrations along the centerline in the 35 atm flame are depleted by 18% by $z = 0$.

As shown in Fig. 7, the concentration of C_2H_2 inside the fuel tube increases as pressure is increased and C_2H_4 breakdown accelerates. Initially, only a small amount of C_2H_2 is present inside the fuel tube at 10 atm. However, concentrations of C_2H_2 near the wall and inside the tube increase significantly with pressure. At 35 atm, C_2H_2 produced near the walls is completely consumed upstream of the fuel tube exit plane. This results in the predicted appearance of soot inside the fuel tube in Fig. 5. The peak concentrations of C_2H_2 are observed to occur along the centerline higher up in the flame. These peak concentrations decrease significantly as pressure is increased. As already discussed by Liu et al. [13], this is a result of increased soot production rates with increasing pressure. This observed decrease in C_2H_2 concentration was also hypothesized to be the cause of decreased sooting propensity with increasing pressure [13]. As pressure is increased and more C_2H_2 is converted to soot, less gaseous carbon mass is available for further soot production.

The flow streamlines are also depicted in Fig. 7. Increasing pressure from 10 to 35 atm is observed to drastically alter the streamlines, causing the flow to contract inwards towards the centerline. At 35 atm, the streamlines near the fuel tube are almost parallel to the top surface. A small region just downstream of the fuel tube in the 10 atm flame exists along the centerline where the streamlines diverge. This region becomes larger and moves inside the fuel tube as pressure is increased and is a direct result of the sudden expansion at the burner exit.

A closeup of the streamlines near the burner exit is provided in Fig. 8 for the 35 atm flame. The coflow streamlines makes a 90° turn towards the fuel stream just prior to exiting the burner. The oxidizer stream eventually flows into the fuel tube which would explain the early oxidation of fuel inside the tube observed at high pressures. This slight inward dip was not observed in the lower pressure flames.

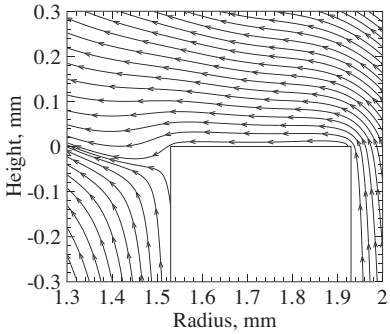

Fig. 8. Streamlines near the fuel tube wall at 35 atm.

6. Conclusions

Although large discrepancies were observed between predictions and measurements for soot volume fraction, the soot model employed in this study predicted the overall features and displayed the correct trends with pressure. In the experiments, the flame height was independent of pressure and the flame diameter decreased with

increasing pressure. Both of these phenomena were correctly predicted by the numerical model. Soot volume fractions were generally over-predicted everywhere in the flame, but the soot model still captured the general trend of increasing carbon conversion factor with pressure. The soot model predicted the appearance of soot much earlier in the flame than observed in the experiments and that soot is formed inside the fuel tube above 20 atm. It has been shown that this soot formation is related to accelerated fuel pyrolysis triggered by enhanced air entrainment and increasing temperatures inside the tube as pressure was increased. As a result, C_2H_2 levels inside the tube intensified with pressure and the C_2H_2-based soot model has incorrectly translated this to an increase in soot production.

The results of this study also illustrated the strong effect of the burner wall on flame structure and its increasing impact with pressure. When studying high pressure laminar flames, inlet boundary placement must be far enough upstream to capture the fuel preheat effect and minimize its impact on the solution.

Future work will include more detailed gas-phase kinetic mechanisms that describe the formation of large molecular weight soot precursors and more realistic models for soot [40,7]. The detailed features of the burner geometry and a conjugate heat transfer analysis of the tube wall will also be included in future efforts.

Acknowledgements

Operational funds for this work have been provided by the Natural Sciences and Engineering Research Council (NSERC) and the Canadian Space Agency (CSA). Computational resources for performing all of the calculations reported herein were provided by the SciNet High Performance Computing Consortium at the University of Toronto and Compute/Calcul Canada through funding from the Canada Foundation for Innovation (CFI) and the Province of Ontario, Canada.

References

[1] W.L. Flower, C.T. Bowman, *Proc. Combust. Inst.* 21 (1988) 1115–1124.
[2] W. Lee, Y.D. Na, *J. Soc. Mech. Eng. Int. J. Ser. B* 43 (2000) 550–555.
[3] L.L. McCrain, W.L. Roberts, *Combust. Flame* 140 (2005) 60–69.
[4] K.A. Thomson, Ö.L. Gülder, E.J. Weckman, R.A. Fraser, G.J. Smallwood, D.R. Snelling, *Combust. Flame* 140 (2005) 222–232.
[5] H.I. Joo, Ö.L. Gülder, *Proc. Combust. Inst.* 32 (2009) 769–775.
[6] D.S. Bento, K.A. Thomson, Ö.L. Gülder, *Combust. Flame* 145 (2006) 765–778.
[7] A. D'Anna, J.H. Kent, *Combust. Flame* 152 (2008) 573–587.
[8] S.B. Dworkin, M.D. Smooke, V. Giovangigli, *Proc. Combust. Inst.* 32 (2009) 1165–1172.
[9] Q. Zhang, M.J. Thomson, H. Guo, F. Liu, G.J. Smallwood, *Combust. Flame* 156 (2009) 697–705.
[10] H. Guo, K.A. Thomson, G.J. Smallwood, *Combust. Flame* 156 (2009) 1135–1142.
[11] R.S. Mehta, D.C. Haworth, M.F. Modest, *Proc. Combust. Inst.* 32 (2009) 1327–1334.
[12] Z. Zhang, O.A. Ezekoye, *Combust. Sci. Technol.* 137 (1998) 323–346.
[13] F. Liu, K. Thomson, H. Guo, G.J. Smallwood, *Combust. Flame* 146 (2006) 456–471.
[14] H. Guo, F. Liu, G.J. Smallwood, Ö.L. Gülder, *Combust. Theor. Model.* 6 (2002) 173–187.
[15] D.R. Snelling, K.A. Thomson, G.J. Smallwood, Ö.L. Gülder, E.J. Weckman, R.A. Fraser, *AIAA J.* 40 (2002) 1789–1795.
[16] M.R.J. Charest, C.P.T. Groth, Ö.L. Gülder, Numerical prediction of sooting laminar diffusion flames using adaptive mesh refinement, in: *Proceedings of the Sixth US National Combustion Meeting*, Ann Arbor, Michigan, Paper 23H4, 2009.
[17] M.R.J. Charest, C.P.T. Groth, Ö.L. Gülder, A computational framework for predicting laminar reactive flows with soot formation, Combust. Theor. Model., in press, doi:10.1080/1364783.2010.512960.
[18] K.K. Kuo, *Principles of Combustion*, second ed., John Wiley & Sons Inc., New Jersey, 2005.
[19] K.M. Leung, R.P. Lindstedt, W.P. Jones, *Combust. Flame* 87 (1991) 289–305.
[20] F. Liu, H. Guo, G.J. Smallwood, Ö.L. Gülder, *J. Quant. Spectrosc. Radiat. Transfer* 73 (2002) 409–421.
[21] J.O. Hirschfelder, C.F. Curtiss, R.B. Byrd, *Molecular Theory of Gases and Liquids*, John Wiley & Sons, New York, 1969.
[22] M.D. Smooke, C.S. McEnally, L.D. Pfefferle, R.J. Hall, M.B. Colket, *Combust. Flame* 117 (1999) 117–139.
[23] I.M. Kennedy, W. Kollmann, J.Y. Chen, *Combust. Flame* 81 (1990) 73–85.
[24] B.G. Carlson, K.D. Lathrop, in: H. Greenspan, C.N. Kelber, D. Okrent (Eds.), *Computing Methods in Reactor Physics*, Gordon and Breach, London, 1968, pp. 171–266.
[25] C.P. Thurgood, A. Pollard, H.A. Becker, *J. Heat Transfer* 117 (1995) 1068–1070.
[26] F. Liu, G.J. Smallwood, Ö.L. Gülder, *J. Thermophys. Heat Transfer* 14 (2000) 278–281.
[27] F. Liu, G.J. Smallwood, Ö.L. Gülder, *Int. J. Heat Mass Transfer* 43 (2000) 3119–3135.
[28] F. Liu, H. Guo, G.J. Smallwood, *Combust. Flame* 138 (2004) 136–154.
[29] A. Soufiani, J. Taine, *Int. J. Heat Mass Transfer* 40 (1997) 987–991.
[30] F. Liu, G.J. Smallwood, Ö.L. Gülder, *J. Quant. Spectrosc. Radiat. Transfer* 68 (2001) 401–417.
[31] V. Goutière, A. Charette, L. Kiss, *Numer. Heat Transfer Pt. B* 41 (2002) 361–381.
[32] S.A. Northrup, C.P.T. Groth, *Solution of laminar combusting flows using a parallel implicit adaptive mesh refinement algorithm, in: Proceedings of the*

Fourth International Conference on Computational Fluid Dynamics, ICCFD4, Ghent, Belgium, pp. 341–346.
[33] X. Gao, C.P.T. Groth, *Int. J. Comput. Fluid Dynam.* 20 (2006) 349–357.
[34] P.L. Roe, *J. Comput. Phys.* 43 (1981) 357–372.
[35] W.J. Coirier, K.G. Powell, *AIAA J.* 34 (1996) 938–945.
[36] J.M. Weiss, W.A. Smith, *AIAA J.* 33 (1995) 2050–2057.
[37] D.G. Goodwin, *Chem. Vapor Depos. XVI and EUROCVD* 14 (2003) 155–162.
[38] C.K. Law, *Combust. Sci. Technol.* 177 (2005) 845–870.
[39] F.G. Roper, C. Smith, A.C. Cunningham, *Combust. Flame* 29 (1977) 227–234.
[40] J. Appel, H. Bockhorn, M. Frenklach, *Combust. Flame* 121 (2000) 122–136.